Similar Raman spectra to Fig. 5 indicating a graphitic tribological layer were found at different locations of the first retrieval and from four other retrievals [both wrought and cast alloys (*21*)], as well as in pin-on-ball tests. Spatially resolved Raman imaging (fig. S6) indicated a definitive correlation between where the graphitic Raman signal came from and where the tribological layer was present. It should be noted that there is extensive literature evidence for a comparable tribological layer in many other retrievals and in simulator tests.

All of the data indicate that the tribological material has a graphitic content similar to partially graphitic carbon. Although we cannot rule out a small impurity of protein in the tribological layer, the fact that there is minimal nitrogen, that a high sp^2 fraction precludes a high hydrogen content, plus the correlation of the Raman and HREM data as to the structure allow us to infer that the fraction of protein is less than 5%, and any protein present should be considered as partially degraded rather than denatured protein.

There are three immediate consequences of this result—the first two are important for orthopedic applications, whereas the other is an issue for concern. The first is that graphite is a standard solid lubricant that is known to perform well in the presence of water (*31*, *32*) and should operate similarly in vivo. In the tribological region, it will serve this purpose, reducing friction as well as corrosion and wear, similar to solid lubricants in an engine. More than just flash-heating or frictional shear of proteins is leading to this layer; instead major chemical changes are taking place that have been hinted at in the degradation product analyses mentioned earlier. Although we do not know the precise mechanism whereby the graphitic material is formed, it is known that many transition metals (here, probably cobalt) will act as catalysts to eliminate water or ammonia from organic materials (*33*, *34*), similar to the well-known coking of heterogeneous catalysts; fresh metal surfaces exposed by wear should be good catalysts. As a crude estimate, the composition of albumin is $C_{3076}H_{4833}N_{821}O_{919}S_{42,}$ and eliminating water, ammonia (and hydrogen sulfide) would give a nominal composition of $C_{3076}H_{448}$, which is comparable to typical hydrogenated carbon films used to reduce friction. There is extensive evidence for the formation of graphitic material from other carbon allotropes during sliding, so a conversion from more disordered or amorphous carbon to a graphitic material is expected.

The second consequence is that there is now a design target for improving implants. For instance, one could design to improve adhesion of the graphitic layer to the metal or to promote its formation by changing the alloy composition and thus reducing wear, friction, and corrosion. Biocompatibility of any additives will be an issue, so the problem is not as simple as designing a better alloy.

Lastly, as a caution, wear of this graphitic material is going to lead to the formation of graphitic fragments in the pseudosynovial fluids, and these can be transported to cells in the nearby regions. The recent finding (*4*) of a lack of correlation between tissue damage and volumetric wear rate suggests that factors other than cobalt-alloy wear debris may be contributing to adverse tissue reactions. Graphitic carbon may be one such factor; further research is needed.

In summary, we have presented clear evidence that the tribological layer in MoM hip replacements is primarily graphitic carbon. This material forms a layer that reduces friction as well as wear and corrosion and suggests a route for the design of improved implants, although there might be physiological implications associated with graphitic wear debris in patients.

References and Notes

1. M. W. Brault, J. Hootman, C. G. Helmick, K. A. Theis, B. S. Armour, *Morb. Mortal. Wkly. Rep.* **58**, 421 (2009).
2. Organisation for Economic Co-operation and Development (OECD)/European Union, *Health at a Glance: Europe 2010* (OECD Publishing, Paris, 2010).
3. K. J. Bozic *et al.*, *J. Bone Joint Surg. Am.* **91**, 128 (2009).
4. D. J. Langton *et al.*, *J. Bone Joint Surg. Br.* **93-B**, 164 (2011).
5. S. A. Jacobsson, K. Djerf, O. Wahlström, *Clin. Orthop. Relat. Res.* **329**, S60 (1996).
6. M. A. Wimmer, J. Loos, R. Nassutt, M. Heitkemper, A. Fischer, *Wear* **250**, 129 (2001).
7. D. Dowson, C. M. McNie, A. A. J. Goldsmith, *Proc. Inst. Mech. Eng. C* **214**, 75 (2000).
8. S. C. Scholes, A. Unsworth, *Proc. Inst. Mech. Eng. H* **214**, 49 (2000).
9. S. C. Scholes, A. Unsworth, *Proc. Inst. Mech. Eng. H* **220**, 687 (2006).
10. A. Unsworth, *Phys. Med. Biol.* **23**, 253 (1978).
11. M. A. Wimmer, C. Sprecher, R. Hauert, G. Tager, A. Fischer, *Wear* **255**, 1007 (2003).
12. Y. Yan, A. Neville, D. Dowson, *J. Phys. D* **39**, 3206 (2006).
13. M. P. Heuberger, M. R. Widmer, E. Zobeley, R. Glockshuber, N. D. Spencer, *Biomaterials* **26**, 1165 (2005).
14. M. A. Wimmer *et al.*, *J. Orthop. Res.* **28**, 436 (2010).
15. V. K. Maskiewicz, P. A. Williams, S. J. Prates, J. G. Bowsher, I. C. Clarke, *J. Biomed. Mater. Res. B Appl. Biomater.* **94**, 429 (2010).
16. H. Mishina, M. Kojima, *Wear* **265**, 655 (2008).
17. F. W. Chan *et al.*, *Clin. Orthop. Relat. Res.* **333**, 96 (1996).
18. H. McKellop *et al.*, *Clin. Orthop. Relat. Res.* **329**, S128 (1996).
19. J. Fink *et al.*, *Solid State Commun.* **47**, 687 (1983).
20. S. D. Berger, D. R. Mckenzie, P. J. Martin, *Philos. Mag. Lett.* **57**, 285 (1988).
21. Materials and methods are available as supporting material on *Science* Online.
22. A. M'ndange-Pfupfu, O. Eryilmaz, A. Erdemir, L. D. Marks, *Diamond Relat. Mater.* **20**, 1143 (2011).
23. J. J. Cuomo, J. P. Doyle, J. Bruley, J. C. Liu, *Appl. Phys. Lett.* **58**, 466 (1991).
24. D. L. Pappas *et al.*, *J. Appl. Phys.* **71**, 5675 (1992).
25. R. F. Egerton, *Electron Energy-Loss Spectroscopy in the Electron Microscope* (Plenum Press, New York, ed. 2, 1996).
26. J. Robertson, *Mater. Sci. Eng. Rep.* **37**, 129 (2002).
27. A. C. Ferrari, J. Robertson, *Phys. Rev. B* **61**, 14095 (2000).
28. A. C. Ferrari, J. Robertson, *Philos. Trans. R. Soc. London Ser. A* **362**, 2477 (2004).
29. F. Tuinstra, J. L. Koenig, *J. Chem. Phys.* **53**, 1126 (1970).
30. P. K. Chu, L. H. Li, *Mater. Chem. Phys.* **96**, 253 (2006).
31. S. K. Field, M. Jarratt, D. G. Teer, *Tribol. Int.* **37**, 949 (2004).
32. B. K. Yen, *Wear* **192**, 208 (1996).
33. J. L. Woodman, J. Black, S. A. Jiminez, *J. Biomed. Mater. Res.* **18**, 99 (1984).
34. A. Kocijan, I. Milosev, B. Pihlar, *J. Mater. Sci. Mater. Med.* **14**, 69 (2003).

Acknowledgments: This work was funded by the NIH on grant number 1RC2AR058993-01. Northwestern University Atomic and Nanoscale Experimental Center and Biological Imaging Facility are acknowledged for the use of their facilities. We thank K. Shull, K. Wahl, and R. Leapman for invaluable comments and M. Morlock, Hamburg, Germany, for retrievals. The authors have no competing financial interests. As full disclosure of real or potential conflicts of interest, J.J.J. has funding from Zimmer Holdings, Medtronics, and Spinal Motion; consults for Zimmer, Medtronics, Johnson and Johnson, Spinal Motion, and Implant Protection; and has stock options in Implant Protection. A.F. has funding from Zimmer Winterthur and consults for Zimmer, Abbot Vascular, and Ceramtec.

Supporting Online Material

www.sciencemag.org/cgi/content/full/334/6063/1687/DC1
Materials and Methods
Figs. S1 to S6

12 September 2011; accepted 1 November 2011
10.1126/science.1213902

Evidence from Numerical Experiments for a Feedback Dynamo Generating Mercury's Magnetic Field

Daniel Heyner,[1]* Johannes Wicht,[2]† Natalia Gómez-Pérez,[3]† Dieter Schmitt,[2] Hans-Ulrich Auster,[1] Karl-Heinz Glassmeier[1,2]

The observed weakness of Mercury's magnetic field poses a long-standing puzzle to dynamo theory. Using numerical dynamo simulations, we show that it could be explained by a negative feedback between the magnetospheric and the internal magnetic fields. Without feedback, a small internal field was amplified by the dynamo process up to Earth-like values. With feedback, the field strength saturated at a much lower level, compatible with the observations at Mercury. The classical saturation mechanism via the Lorentz force was replaced by the external field impact. The resulting surface field was dominated by uneven harmonic components. This will allow the feedback model to be distinguished from other models once a more accurate field model is constructed from MErcury Surface, Space ENvironment, GEochemistry, and Ranging (MESSENGER) and BepiColombo data.

In March 2011, the MErcury Surface, Space ENvironment, GEochemistry, and Ranging (MESSENGER) mission (*1*) entered orbit around Mercury. One of its objectives is to explore the planet's magnetic field, which is presumed to be generated by a dynamo operating

in the liquid iron core. However, the magnetic field created by a classical convectively driven dynamo—like the one operating inside Earth—would be one to two orders of magnitude stronger (*2*, *3*) than actually inferred from spacecraft flybys so far (*4*). To explain this discrepancy, several dynamo models have been suggested, which rely on a particular interior structure or invoke a completely different mechanism [for overviews, see (*3*, *5*)].

All of these models neglect the magnetospheric field, which may reach sizable values even at the planet's core-mantle boundary because the magnetopause lies very close to Mercury's surface. It has been suggested that the negative feedback between the magnetospheric and internal magnetic fields may actually be the reason for the low field amplitude (*6*–*10*). Because Mercury's dynamo region is not directly accessible, numerical simulations provide the only way to test the feasibility of this idea. Here, we present fully self-consistent, three-dimensional (3D) magnetohydrodynamic dynamo models that invoke a dynamical coupling between the internal dynamo process and the magnetospheric field.

Mercury, the innermost planet in the solar system, is subject to an intense solar-wind flux. The interaction of the impinging solar wind with the planetary dipole field creates a magnetopause current layer separating the magnetosphere from interplanetary space. Its distance from the planet is mainly determined by the equilibrium between the solar-wind momentum flux outside and the magnetic pressure of the compressed dipole field inside the magnetopause. Mercury's weak dipole field can barely push the magnetopause beyond the planetary surface. Therefore, the external field contributes substantially to the overall field within the magnetosphere (*6*, *11*, *12*) and the planet's interior. At the core-mantle boundary, external and internal dipole fields are inherently antiparallel (Fig. 1). The external field diffuses into the conducting core with a penetration depth that depends on its time scale. A constant and uniform field would have completely penetrated a stagnant core after about one magnetic diffusion time of ~35,000 years for Mercury (*13*). Fast solar- and orbit-induced variations are therefore negligible, and the magnetospheric field can be approximated by an axial, uniform field (*6*).

The first feedback models employed simple kinematic, 1D mean-field dynamos and simple parameterized magnetopause fields (*6*, *9*, *10*). In a second step, full numerical dynamo simulations were subjected to a constant imposed external field (*8*). In a third step, the external field was set to switch polarity, so that it always opposed the internal dipole direction, but its amplitude was kept constant (*7*). These approaches demonstrated that the external field can indeed have an important effect on the internal mechanism and may lower the overall field strength. However, these inherent simplifications substantially limited the predictive power for Mercury.

Our approach included a dynamical coupling between the full 3D internal dynamo model MagIC (*14*, *15*) with an external magnetospheric field model. The functional dependence of the external field on the internal field was based on magnetospheric field modeling (*9*, *16*), which suggests that the external field remains constant when the magnetospheric stand-off distance is large enough. However, the model external field strength decreases once the magnetopause comes close enough to the surface that the planet physically limits its extent. We chose the functional form $g^0_{1,\mathrm{ext}} = \alpha \cdot \mathrm{sgn}(g^0_{1,\mathrm{int}}) \frac{|g^0_{1,\mathrm{int}}|^5}{\beta^5 + |g^0_{1,\mathrm{int}}|^5}$ where $g^0_{1,\mathrm{ext}}$ and $g^0_{1,\mathrm{int}}$ are the external and total internal axial dipole Gauss coefficients (*17*), respectively, and α and β are parameters, with the unit Tesla, that both define the shape of the response function.

The internal dynamo model is characterized by the five dimensionless control parameters $Ra = 7.5 \times 10^6$, $E = 10^{-4}$, $Pm = 2/3$, $Pr = 1$ and $\chi = 0.35$ (*14*, *15*). The Rayleigh number Ra is a measure for the convective driving of the system. The Ekman number (E) represents for the relative importance of viscous to Coriolis forces. We chose a moderately small value of E to damp the small-scale convection that we could not afford to resolve numerically for the large number of simulations we performed. The large E value forced us to also use a large magnetic Prandtl number (Pm), the ratio of viscous to magnetic diffusivity, to guarantee dynamo action (*18*) at the Rayleigh number we chose. The Rayleigh number was adjusted so that our reference case without feedback yielded a dipole-dominated internal field that grew slowly from a small seed field (i.e., the reference dynamo was supercritical with respect to the onset of dynamo action). This is typically the case when an intermediate Rayleigh number is chosen. Dynamos at small Rayleigh numbers may be subcritical; that is, they do not amplify a weak field. When Ra is too large, dynamos tend to produce nondipolar fields (*19*), and the convection is too vigorous for the feedback to play any role (*9*). Our Prandtl number (Pr), the ratio of viscous to thermal diffusivity, is appropriate for thermal core convection. Because the ratio of the inner- to outer-core radius χ is yet unconstrained for Mercury (*20*), we adopted $\chi = 0.35$ to facilitate a comparison with Earth-like simulations. Although some of these parameters do not reflect the real situation, their respective dynamo models nevertheless yield realistic planetary-field behavior (*21*).

Without a magnetic field, the forces on convective flows in fast rotating systems (these with a small Ekman number) obey the geostrophic force balance where only Coriolis, pressure gradient, and buoyancy forces contribute in leading order. A key property of geostrophic flows is the minimized variation in the z direction, the direction along the rotation axis, formulated by the Proudman-Taylor theorem. We measured the degree of geostrophy in the system by determining the kinetic energy G carried by the z-averaged flow relative to the total kinetic energy. In the purely convective model without a magnetic field, we found $G \approx 0.47$. In planetary dynamos (that is, those with a magnetic field), the Lorentz force also enters the leading-order force balance, which is then called magnetostrophic. The strong Lorentz force may then release the Proudman-

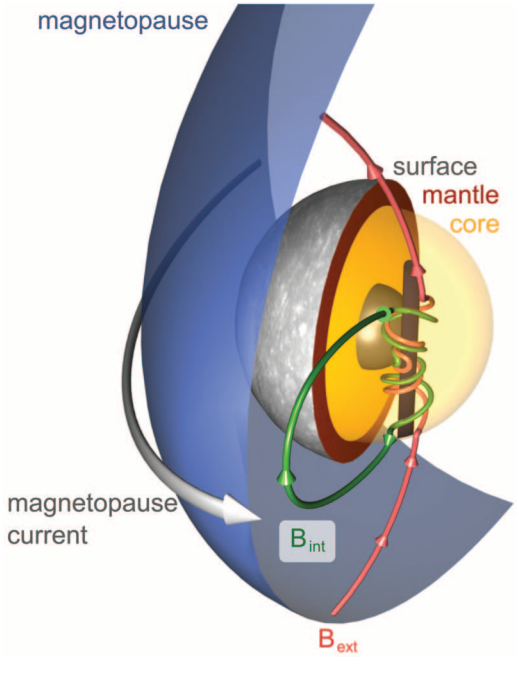

Fig. 1. The feedback dynamo mechanism. Mercury is in the center, and the solar wind enters from the lower-left corner. The magnetopause is created as a result of the interaction with the planetary dipole field B_{int}. The external field B_{ext} due to the magnetopause current reaches through the planetary mantle and enters the fluid outer core. There, the dynamo dipole field and the external field are antiparallel. The anticyclones (brown column) in the core convert the poloidal field into an azimuthal one, stretch it at the same time due to a secondary poleward flow away from the equator, and thereby enhance the field amplitude. At this point, internal and external fields become mixed and weaken each other.

[1]Institut für Geophysik und extraterrestrische Physik, Technische Universität, Braunschweig, Germany. [2]Max-Planck-Institut für Sonnensystemforschung, Katlenburg-Lindau, Germany. [3]Departamento de Física, Universidad de los Andes, Bogota, Colombia.

*To whom correspondence should be addressed. E-mail: d.heyner@tu-braunschweig.de

†These authors contributed equally to this work.

Taylor constraint and allow for more z dependence. The Elsasser number Λ is a diagnostic parameter for the ratio of Lorentz to Coriolis forces, and a value of ~1 is seen as indicative of the magnetostrophic regime [see, for example, (*18*) for a discussion]. In this regime, the Lorentz force is strong enough to sufficiently change the convective flow and establish saturation by limiting the otherwise quasi-exponential magnetic-field growth. A Λ close to 1 has been found to hold for Earth, Jupiter, Saturn (*22*), and typical convective dynamo simulations like our reference model. In our no-feedback reference case, Λ grew from a weak seed field $\Lambda_{init} \approx 10^{-4}$ and saturated at about the magnetostrophic balance with $\Lambda \approx 1$ (Fig. 2, case a). The lower respective geostrophy measure of $G \approx 0.36$ demonstrates that the constraint imposed by the Proudman-Taylor theorem is indeed released.

When the external field was present, the evolution of the dynamo was substantially altered. The relative response function $g^0_{1,ext}/g^0_{1,int}$ is the determining factor (*10*), and the parameter α sets the maximum amplitude of this ratio. For sufficiently large values of α, the dynamo saturates early at a weak magnetic energy level, with a characteristic $g^0_{1,ext}/g^0_{1,int}$ ratio of 0.1 . For α_1 = 70 nT and β = 96 nT, the relative response function resembled qualitatively that derived from simple scaling of the terrestrial magnetosphere to Hermean conditions (*9*), and it ensures a smooth transition at the origin (Fig. 2, right). Eventually, for this feedback-stabilized dynamo, the Elsasser number remained below 10^{-5} (Fig. 2, case b). The Lorentz force was then too weak to substantially modify the convective flow, which therefore remained in the geostrophic regime. The stabilization worked successfully for different strengths of the external field, α, but failed when we decreased it to α_2 = 19 nT; then the solution evolved again into the magnetostrophic state (Fig. 2, case c). Our experiments also showed that stronger dynamo action required a higher value of α to still quench the dynamo growth. We validated the saturation mechanism through the negative feedback by removing the imposed field from the already weak case (Fig. 2, case d). Again, this dynamo evolved toward the magnetostrophic balance, demonstrating the restraining influence of the feedback on the dynamo.

The Lorentz force in strong-field dynamos leads to large convective flow structures (Fig. 3) with vorticity columns that radially stretch further out into the shell (*23*, *24*). Because of the small Lorentz force, the flow in the feedback dynamo exhibited smaller scales and resembled the structures of the nonmagnetic case. Consequently, the Lorentz force was also too weak to establish magnetic field saturation and the role was taken over by the negative external feedback, which directly limited the efficiency of magnetic induction. The magnetic field strength was now determined by the balance between Ohmic dissipation and the less effective magnetic field production. Scaled to Mercury values, the total internal dipole strength amounted to ~60 nT with 10% magnetospheric contribution. This internal dipole strength was substantially lower than those in previous simplified feedback dynamo attempts (*7*).

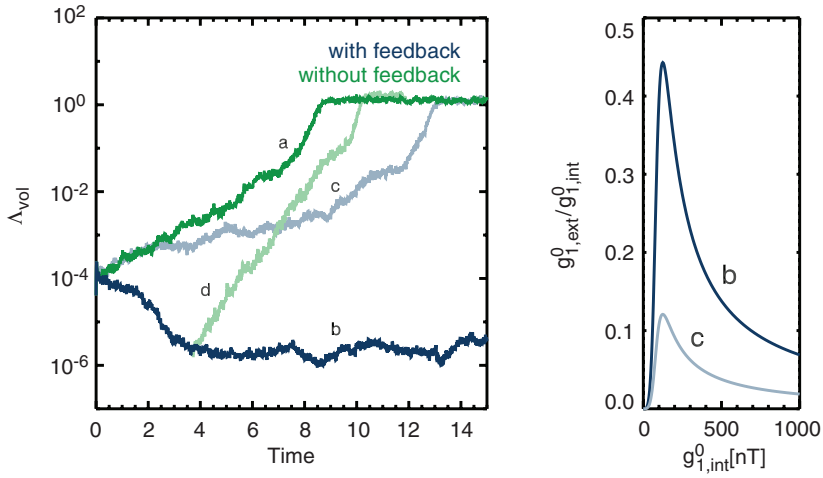

Fig. 2. (**Left**) Volume-averaged Elsasser number (Λ_{vol}) versus time. Time is in units of a magnetic diffusion time. Blue and green lines mark the Elsasser number for the cases with and without feedback, respectively. Letters: a, reference case without external field; b, feedback-stabilized dynamo; c, same dynamo as b but with a lower amplitude of the external field; d, control case (restart of b with external field turned off, saturating at $\Lambda \approx 1$). (**Right**) Ratio of external to internal dipole fields versus the internal dipole field at the planetary surface for the two cases shown on the left with external field.

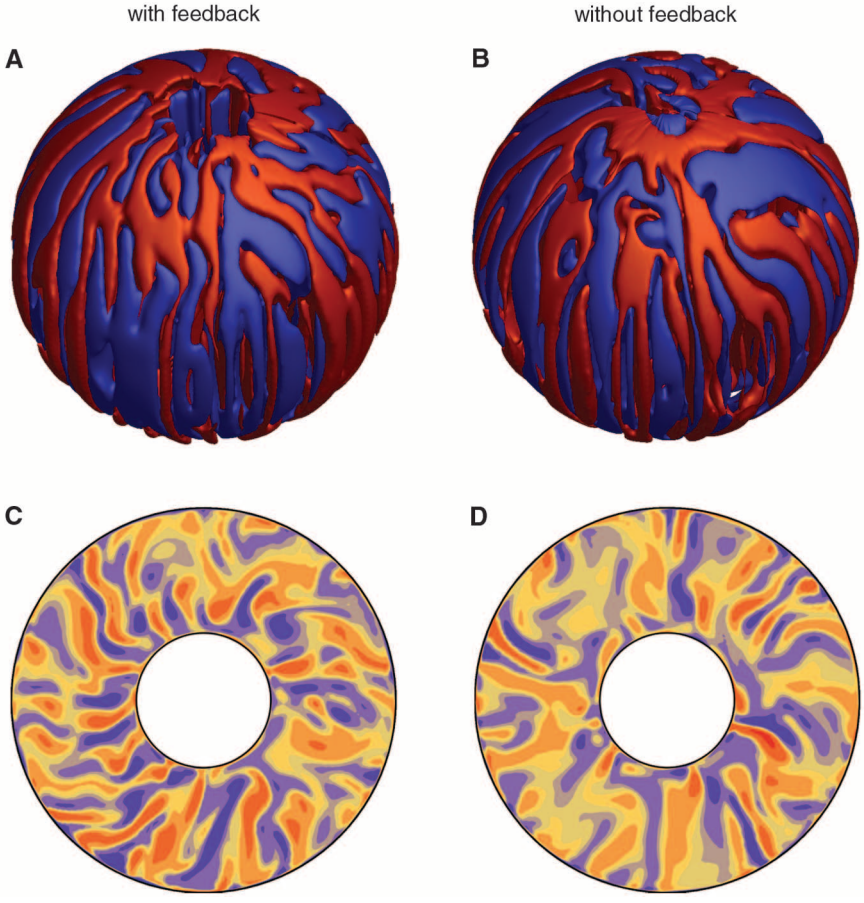

Fig. 3. (**A** to **D**) z vorticity in simulations with (left) and without (right) feedback. Red and blue color corresponds to positive and negative vorticity, respectively. Isosurfaces of z vorticity at the core-mantle boundary (top) and in an equatorial cut (bottom).

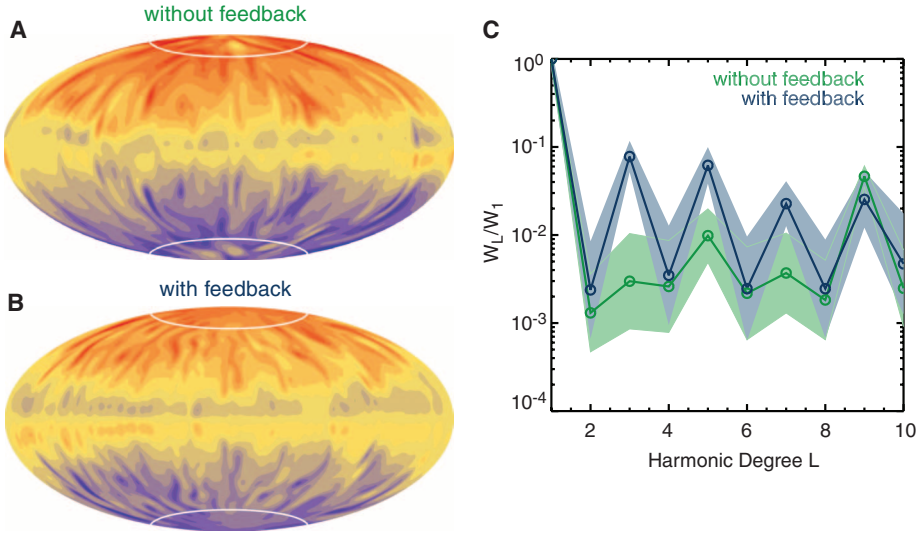

Fig. 4. (**A** and **B**) Hammer projections of the radial magnetic field component at the core-mantle boundary. Red color illustrates an outward-directed field; blue denotes an inward-directed field. White lines mark the intersection of the tangent cylinder with the core-mantle boundary. (A) Simulation without feedback; (B) with feedback (**C**) Mauersberger-Lowes spectrum (*17*) at the planetary surface normalized to the dipolar (l = 1) mode. The blue and green lines mark the case with and without feedback, respectively. The shaded area illustrates the logarithmic standard deviation from the mean; the spectra have been averaged over time for $t \geq 10$ magnetic diffusion times.

The geostrophy of the flow has consequences for the magnetic field topology at the core-mantle boundary (Fig. 4, A and B). The feedback-induced weak-field solution exhibits intense magnetic field spots near the rotation poles. In the magnetostrophic case, the convective features radially extend outward in a more undisturbed manner; thus, stronger magnetic field patches can also be found at lower latitudes. The magnetic energy spectra at the planetary surface both show a clear dominance of the dipole component (Fig. 4C). The weak-field solution has more pronounced uneven components in the spectrum than the reference strong-field solution, which corresponds to field concentrations at higher latitudes. The ratio between the dipole and quadrupole is mainly controlled by the underlying dynamo model. Beyond a certain Rayleigh number, the dipole loses its dominance and becomes comparable to the quadrupole contribution, or higher spherical harmonics. The alternative models generally show different spectra. If the dynamo is buried beneath a nonconvecting layer (*25*), the quadrupole component is predicted to be as strong as the dipole component. Models relying on a large solid inner core (*26*, *27*) or a double-snow state (*28*) also exhibit pronounced uneven harmonics, but they show distinct magnetic flux concentrations at lower latitudes that are not present in our model with an Earth- like inner-core size. This results in different dipole-to-quadrupole ratios among the models. The lack of strong flux patches at lower latitudes may offer another distinguishing feature of our model.

The feedback mechanism can only succeed in establishing a weak-field state when the internal field is very weak to start with, most likely in the start-up phase of supercritical dynamo action. Planets have probably started their evolution rather hot with vigorous core convection driving a strong-field dynamo. The giant impact responsible for the Caloris basin on Mercury, however, may have caused a temporary dynamo shutdown (*29*). The planet's thermal history offers another scenario. Today's heat flux through Mercury's core-mantle boundary is possibly subadiabatic, which means that the only way to drive a dynamo is via the latent heat and the release of light elements from the surface of a growing inner core (*3*). However, simulations of the planet's thermal history suggest that the heat flux may have become subadiabatic even before the inner core started to form (*30*). Thus, the start of inner-core crystallization may have revitalized Mercury's already dead dynamo.

The MESSENGER mission will return more magnetic field data from which higher internal harmonic field coefficients can be inferred (*31*). The dual-spacecraft BepiColombo mission (*32*) to be launched in 2014 will provide further information on the internal magnetic field, as it allows a detailed separation of the internal field from the magnetospheric contributions (*17*, *33*). These improved magnetic field measurements will facilitate a more detailed comparison to the predictions of dynamo models derived from numerical experiments aimed to explain the enigmatic weakness of the magnetic field of Mercury.

References and Notes

1. S. C. Solomon, R. L. McNutt Jr., R. E. Gold, D. L. Domingue, *Space Sci. Rev.* **131**, 3 (2007).
2. P. Olson, U. R. Christensen, *Earth Planet. Sci. Lett.* **250**, 561 (2006).
3. J. Wicht *et al.*, *Space Sci. Rev.* **132**, 261 (2007).
4. B. J. Anderson *et al.*, *Space Sci. Rev.* **152**, 307 (2010).
5. S. Stanley, G. A. Glatzmaier, *Space Sci. Rev.* **152**, 617 (2010).
6. K.-H. Glassmeier, H.-U. Auster, U. Motschmann, *Geophys. Res. Lett.* **34**, L22201 (2007).
7. N. Gómez-Pérez, S. C. Solomon, *Geophys. Res. Lett.* **37**, L20204 (2010).
8. N. Gómez-Pérez, J. Wicht, *Icarus* **209**, 53 (2010).
9. D. Heyner *et al.*, *Geophys. Astrophys. Fluid Dyn.* **104**, 419 (2010).
10. D. Heyner, D. Schmitt, K.-H. Glassmeier, J. Wicht, *Astron. Nachr.* **332**, 36 (2011).
11. J. Grosser, K.-H. Glassmeier, A. Stadelmann, *Planet. Space Sci.* **52**, 1251 (2004).
12. C. L. Johnson *et al.*, *Lunar Planet. Sci. Conf.* **40**, 1385 (abstr.) (2009).
13. The magnetic diffusion time is given by $\mu_0 \sigma L^2$. We assumed a core conductivity of $\sigma = 6 \times 10^5$ S/m (*34*), a vacuum magnetic permeability μ_0, and $L = R_{cmb} - R_{icb}$ as the thickness of the dynamo region, with R_{cmb} = 1860 km as the radius of the core-mantle boundary (*35*). The inner core radius R_{icb} is not well-constrained; we chose an Earth-like value of $0.35 R_{cmb}$.
14. J. Wicht, *Phys. Earth Planet. Inter.* **132**, 281 (2002).
15. U. Christensen, J. Wicht, *Treatise on Geophysics*, G. Schubert, Ed. (Elsevier, Oxford, 2007).
16. H. Korth *et al.*, *Planet. Space Sci.* **52**, 733 (2004).
17. N. Olsen, K.-H. Glassmeier, X. Jia, *Space Sci. Rev.* **152**, 135 (2010).
18. U. R. Christensen, J. Aubert, *Geophys. J. Int.* **166**, 97 (2006).
19. U. R. Christensen, J. Aubert, G. Hulot, *Earth Planet. Sci. Lett.* **296**, 487 (2010).
20. D. Breuer, S. Labrosse, T. Spohn, *Space Sci. Rev.* **152**, 449 (2010).
21. J. Wicht, S. Stellmach, H. Harder, *Numerical Dynamo Simulations: From Basic Concepts to Realistic Models* (Springer, Berlin, 2010).
22. G. Schubert, K. M. Soderlund, *Phys. Earth Planet. Inter.* **187**, 92 (2011).
23. A. Sakuraba, P. H. Roberts, *Nat. Geosci.* **2**, 802 (2009).
24. K. Hori, J. Wicht, U. R. Christensen, *Phys. Earth Planet. Inter.* **182**, 85 (2010).
25. U. R. Christensen, *Nature* **444**, 1056 (2006).
26. S. Stanley, J. Bloxham, W. E. Hutchison, M. T. Zuber, *Earth Planet. Sci. Lett.* **234**, 27 (2005).
27. F. Takahashi, M. Matsushima, *Geophys. Res. Lett.* **33**, L10202 (2006).
28. R. Vilim, S. Stanley, S. A. Hauck II, *J. Geophys. Res.* **115**, E11003 (2010).
29. J. Arkani-Hamed, A. Ghods, *Icarus* **212**, 920 (2011).
30. D. Breuer, S. A. Hauck II, M. Buske, M. Pauer, T. Spohn, *Space Sci. Rev.* **132**, 229 (2007).
31. H. Uno, C. L. Johnson, B. J. Anderson, H. Korth, S. C. Solomon, *Earth Planet. Sci. Lett.* **285**, 328 (2009).
32. J. Benkhoff *et al.*, *Planet. Space Sci.* **58**, 2 (2010).
33. K.-H. Glassmeier *et al.*, *Planet. Space Sci.* **58**, 287 (2010).
34. S. T. Suess, B. E. Goldstein, *J. Geophys. Res.* **84**, 3306 (1979).
35. T. Spohn, F. Sohl, K. Wieczerkowski, V. Conzelmann, *Planet. Space Sci.* **49**, 1561 (2001).

Acknowledgments: We appreciated fruitful discussions with U. Christensen. The computing resources of the Gesellschaft für wissenschaftliche Datenverarbeitung (GWDG), Germany, and the Norddeutscher Verbund für Hoch- und Höchstleistungsrechnen (HLRN), Germany, are gratefully acknowledged. This work was financially supported by the German Ministerium für Wirtschaft und Technologie and the German Zentrum für Luft- und Raumfahrt under contract 50 QW 1101.

20 April 2011; accepted 10 November 2011
10.1126/science.1207290